Physical Review B 104 (2021) 174415

Room Temperature Magnetoelectricity in Transition Metal Doped Ferroelectrics

Shalini Kumari[1,2], Dhiren K. Pradhan[3,*], Shi Liu[4], M. M. Rahaman[3], Peng Zhou[5] , Dillip K. Pradhan[6], Ashok Kumar[7], Gopalan Srinivasan[5], Ram S. Katiyar[1], and J. F. Scott[8,*]

[1]Department of Physics and Institute for Functional Nanomaterials, University of Puerto Rico, San Juan, PR 00931, USA.
[2]Department of Physics and Astronomy, West Virginia University, Morgantown, WV 26506, USA.
[3]Geophysical Laboratory, Carnegie Institution for Science, Washington, DC 20015, USA.
[4]Army Research Laboratory, Adelphi, MD 20783, USA.
[5]Physics Department, Oakland University, Rochester, Michigan 48309- 4401, USA.
[6]Department of Physics and Astronomy, National Institute of Technology, Rourkela-769008, India.
[7]CSIR-National Physical Laboratory, Dr. K. S. Krishnan Marg, New Delhi 110012, India.
[8]Department of Chemistry and Department of Physics, University of St. Andrews, St. Andrews KY16 ST, U. K.

Abstract

There are increasing activities in search of novel single-phase magnetoelectric (ME) materials those exhibit strong ME coupling at room temperature for the ultimate memory, spintronics, and other multifunctional devices, by making use of the ability of controlling polarization by a magnetic field and/or magnetization by an electric field. Obtaining single-phase ME materials with strong ME coupling, understanding its origin, and manipulating the processing and composition to realize large ME coefficients at room temperature constitute the holy grail of multiferroic research and remain difficult to achieve until now. In continuation of our search for better ME materials, we have investigated the multiferroic and ME properties of Ni-doped $Pb(Zr_{0.20}Ti_{0.80})O_3$. We find that the ferroelectric ($T_c \sim 700K$) and weak ferromagnetic (~ 602 K) phase transitions of Ni-doped PZT are well above room temperature, leading to a strong ME coupling coefficient ($\alpha_{E,31}$) of 1.25 mV/cm.Oe which increases to 11.7 mV/cm.Oe with increase of frequency from 30 Hz to 1 kHz. We further demonstrate that Ni-doped PZT exhibits low loss tangent, low leakage current, large saturation polarization and weak ferromagnetism. Ultimately, our work demonstrates Ni-PZT is a cost-effective room-temperature single-phase multiferroic with strong ME coupling.

*Authors to whom correspondence to be addressed. Electronic mail: jfs4@st-andrews.ac.uk (J. F. Scott), dhirenkumarp@gmail.com (Dhiren K. Pradhan)

Introduction

Magnetoelectric- Multiferroic (MF) materials exhibiting simultaneous ferroelectric, and ferromagnetic behaviors and permitting control and switching of the magnetization (M) by electric field (E), and polarization (P) via magnetic field (H) have drawn enormous interest because of their fascinating physics and great potential for memory, spintronics, and multifunctional applications.[1-5] Magnetoelectric materials exhibiting robust ME coupling might hold the future for the ultimate memory application for device miniaturization beyond Moore's Law.[3,5,6] Because of the intrinsic incompatibility between magnetism and ferroelectricity in oxide perovskites, only a few single-phase multiferroic oxides exist in nature, such as $BiFeO_3$, $Pb(Fe_{0.5}Nb_{0.5})O_3$, $YMnO_3$, $Pb(Fe_{0.5}Ta_{0.5})O_3$, $Pb(Fe_{0.67}W_{0.33})O_3$, and $TbMnO_3$.[1,7] $BiFeO_3$ (BFO) is the most studied room-temperature lead-free single-phase multiferroic with both ferroelectric and antiferromagnetic critical temperature above room temperature.[8-10] For practical device applications, it is still not optimal, due to its high leakage current and small ME coupling coefficient. Most of the other multiferroic materials exhibit ferroelectric and/or magnetic phase transitions at cryogenic temperatures.[9,11-12] The large difference between the ferroelectric and magnetic ordering temperatures often suggests small ME coupling.[11,12] Realizing strong ME coupling above room temperature in single-phase materials and understanding its origin is vitally important for practical applications.[1,2,11,12] To realize both ferroelectric and magnetic orderings above room temperature with strong ME coupling, composite structures of strong ferroelectric and magnetic materials have been envisioned and produced.[13-17] But for some specific device geometries and applications (such as multiferroic tunnel junctions), single-phase ME materials are necessary because the electrical switching of magnetization is significantly faster in single-phase multiferroics than in composite

materials (where it is strain-coupled and therefore is limited by the speed of sound).[11,12,18-19] Understanding the mechanisms and nature of ME coupling is a long standing research topic in condensed matter physics as it is required for enabling a number of potential devices which make use of controlling electrical order parameters by magnetic field or magnetism via an electric field.[1,2,8,11,18] In continuation to our search for new single-phase multiferroic materials possessing strong ME coupling with both ferroelectric and magnetic phase transitions above room temperature, we have investigated the multiferroic and magnetoelectric properties of Ni doped $Pb(Zr_{0.20}Ti_{0.80})O_3$. $Pb(Zr_{0.20}Ti_{0.80})_{0.70}Ni_{0.30}O_{3-\delta}$ will be abbreviated as PZTNi30 throughout the manuscript. $Pb(Zr_{0.20}Ti_{0.80})O_3$ is one of the best ferroelectric materials with a ferroelectric $T_c \sim 720$ K with high dielectric permittivity, low loss tangent and high piezoelectric coefficient at room temperature, whereas Ni is a transition metal usually having ferromagnetic behavior and is relatively cheap.[12, 2020] PZTNi30 thin films show large polarization and good photovoltaic properties.[21-22] Here we have investigated the structural, ferroelectric, magnetic and ME coupling properties of PZTNi30 ceramics at room temperature. Interestingly, we also found closer proximity and thus apparently less independence between ferroelectric and magnetic ordering temperatures. We find that this material shows strong ME coupling with both ferroelectric and magnetic phase transitions well above room temperature.

Experimental details

Phase-pure PZTNi30 polycrystalline ceramic powders were prepared using high temperature solid-state reaction method from stoichiometric mixture of high purity (> 99.99%) PbO, ZrO_2, TiO_2, and NiO precursors (Alfa Aesar). Mechanical ball milling of all precursors with required stoichiometric amounts was carried out with zirconium balls in methanol media. These powders were calcined in air atmosphere at an optimized temperature of 1373 K for 10 h, using a carbolite

furnace (HTF1700) with a heating rate of 5° K/min. The long-time high-energy, high-temperature ball milling process significantly enhances the chemical processing and single- phase material formation. The phase-pure PZTNi30 powders were pressed into cylindrical pellets of 13 mm diameter, under an isostatic pressure of 5×10^6 Nm^{-2}, using a hydraulic press. The phase formation of the sintered pellets were examined by X-ray diffractometer (Rigaku Ultima III) having a CuK_α radiation source at 40 kV and 40 mA in a slow scan rate of 0. 2° per min. Later the Rietveld refinement was performed with the help of FullProf Suite Software. Field emission scanning electron microscopy (FESEM) images and elemental mapping were recorded utilizing a Zeiss Auriga FESEM equipped with an Oxford Instruments X-Max 80 (SDD) EDS system. Existence of all elements and valence states of the synthesized pellets were confirmed utilizing X-ray fluorescence spectroscopy (XRF) and high-resolution X-ray photoemission spectroscopy (XPS), respectively. Structural analyses were done via temperature-dependent Raman spectroscopy, using a T64000 spectrometer operating in backscattering configuration and in subtractive mode and in addition with XRD. About 8 mW of continuous power from a Coherent argon ion laser (Innova 90 – 5) at 5145 Å was focused to a small spot size of ~ 2 μm^2. A liquid nitrogen-cooled CCD device collected the low and high temperature Raman scattered signal through an 80X objective in vacuum from 83 K to 900 K in steps of 25 K using Linkam TP93 and TMS94 temperature controllers and liquid nitrogen pump cooling module. Both the flat surfaces of the sintered pellets were polished with fine emery papers, and then electrodes were made by painting high purity silver paint, followed by heating at 373 K for 2 h in air for better conduction and adhesion. The dielectric parameters were measured utilizing an HP4294A impedance analyzer under high vacuum (10^{-6} Torr). Thermal control was maintained using a variable temperature micro-probe system equipped with a programmable temperature controller (MMR Technologies,

Inc.) in the range of 80 – 700 K. Ferroelectric properties were measured at room temperature using Radiant RT 6000 High Voltage System after poling the sample under a voltage of 1200 V for 4 h using a DC Power supply (TREK, Inc., Model: 677A). Magnetic properties of the PZTNi30 samples were performed by using a Quantum Design physical properties measurement system (PPMS) DynaCool in a wide range of temperature 300 - 800 K. The dynamic ME measurements were carried out at room temperature utilizing a homemade ME coupling set-up, using a magnet with varying field of up to ± 1500 Oe with a lock-in amplifier and reference ac magnetic field with a Helmholtz coil.

Computational Methods

All density functional theory calculations are carried out using Quantum Espresso with PBEsol density functional approximation and 2×2×2 Monkhorst-Pack sampling.[23] We used ultrasoft pseudopotentials from the Garrity, Bennett, Rabe, Vanderbilt high-throughput pseudopotential set[24] and a plane-wave cutoff of 50 Ryd and a charge density cutoff of 250 Ry. To better describe the *d*-states of Ni, we used the DFT + *U* method where a Hubbard-like *U* term is introduced.[25] The value of *U* is determined by the self-consistent linear-response method[26] implemented in Quantum Espresso. Specifically, we first relax Ni-doped $PbTiO_3$ with lattice constants fixed to experimental values with PBEsol; then we carry out the linear-response approach to estimate the *U* value. For $(Ni_{Pb})^{\times}$, the calculated *U* value is 7.0 eV, and for both $(Ni_{Ti})^{\times}$ and $[(Ni_{Ti}'' - V_O^{\cdot\cdot})^{\times}]$, the *U* value is 9.3 eV. An energy convergence threshold of 1.0×10^{-4} Ry and a force convergence threshold of 1.0×10^{-3} Ry/Bohr and Mazrzari–Vanderbilt smearing of 1 mRy are used to relax fully the atomic positions.

Results and Discussion:

X-ray diffraction

The XRD patterns of PZTNi30 samples were recorded in the 2θ range of 20°- 60° for structural analysis of the material. The presence of sharp diffraction peaks in XRD patterns indicated good homogeneity and crystallization of the samples. A close examination of the XRD patterns further confirms the formation of a single-phase material without appearance of secondary phases or lead-deficient pyrochlore phases. The Rietveld refinement of the XRD patterns was carried out using FULLPROF software package to get the detailed structural information about the material.[27] We have taken the polar space group *P4mm* of tetragonal crystal structure for the refinement. In the unit cell of PZNT with *P4mm* space group, Pb occupies at 1a (0, 0, *z*) site; $Zr^{4+}/Ti^{4+}/Ni^{4+}$ occupies at 1b site (0.5, 0.5, *z*); oxygen O1 at 1b site (0.5, 0.5, *z*); and oxygen O2 at 2c site (0.5, 0, *z*). We have used the Thompson-Cox-Hastings pseudo-Voigt asymmetry function to define the peak profile function, whereas a linear interpolation method was used to describe the background. The adjustable parameters, such as scale factor, zero correction, background, half-width parameter (U, V, W), lattice parameter, and position coordinates have been optimized during the refinement process. The occupancy parameters of the ions were kept fixed during the refinement process. The Rietveld refinement pattern of PZTNi30 is shown in Fig. 1 (a), where the experimental data points are shown as circles and simulated data are shown as solid lines. The difference between experimental and the simulated data are shown at the bottom of the plot, and the vertical lines indicate positions of the Bragg reflections. From this figure it has been observed that there is a good match between the experimental and simulated data with the goodness of fit parameter χ^2 value 1.18. The observed lattice parameters are a = b = 3.9602 (1), c=4.1289 (1) Å with a tetragonality ratio of 1.04, which corresponds to the normal ferroelectric behavior. The appearance

of tetragonality in PZTNi30 is consistent with PZT (20/80), the highly tetragonal Ti-rich system of PZT. All the refined parameters are presented in Table 1 and are well matched with the parent compound.[12,28] From the observed lattice parameters we can state that, there is no change in the basic crystal structure of PZT with substitution of Ni^{2+}.

Scanning Electron Microscopy

As we observed weak ferromagnetic ordering in Ni doped PZT, we have investigated whether Ni is homogeneously distributed or partially segregated in the PZT matrix. To prove the presence of all elements (Pb, Zr, Ti, O, Ni) and to check the surface morphology with elemental mapping of the sintered pellet of PZTNi30, scanning electron microscopy (SEM) was carried out and is shown in Fig. 2 (a). From the SEM image it is observed that the grain growth process is almost completed during the sintering process. Uniform distribution of grains throughout the surface of the sample is observed with well-defined grains and grain boundaries. The microstructures were observed to be dense and homogeneous with a minimum number of holes or cracks. The SEM image revealed the polycrystalline nature of microstructures with grains of different shapes and size ranging between $\sim 1 - 4$ μm. It is clearly evident that all the elements are uniformly distributed in a large area of $\sim 25 \times 25$ μm^2. Ni (green colored) is distributed homogeneously throughout the sample without forming any clusters in a large area. The distribution of Ni is also studied in a single grain of PZTNi30 sample, and we found that in a single grain it is also homogeneously distributed. Hence it can be safely concluded that the magnetic properties observed in our case are not due to extrinsic effects such as the presence of secondary phases or clustering of Ni. The wt % of each element present in PZTNi30 has been calculated and is found to be approximately the same with the wt % of the raw materials used for the synthesis, within experimental limit. The color images illustrate quantitative analyses of materials present in the system.

Calorimetric, dielectric, ferroelectric and leakage current properties:

To get insight into the ferroelectric phase transition behavior, temperature dependence of dielectric permittivity (ε_r) measurements were carried out over a wide range of frequencies (100 Hz - 1 MHz) and are depicted in Fig. 3 (a). The dielectric permittivity (ε_r) decreases with rise in frequency for PZTNi30, which is a characteristic of polar dielectrics. ε_r increases slowly with increase of temperature up to 550 K and then increases rapidly up to 700 K with further increase of temperature. We could not probe the ferroelectric-paraelectric phase transition temperature (T_c) due to experimental limitation. But from this figure it is clear that the ferroelectric T_c of PZTNi30 lies at or above 700 K. We have probed the ferroelectric phase transition of PZTNi30 by Raman spectroscopy measurements that are discussed in the following section. The inset of Fig. 2 (a) shows the loss tangent (tan δ) of PZTNi30 as a function of temperature at different frequencies. The tan δ increases with an increase of temperature, and the increase is more prominent at higher temperature; this might be due to space charge polarization and interfacial polarization across the Ag / PZTNi30 interface.[12, 29] The room-temperature loss tangent is found to be very low (0.009 at 1 kHz), which makes this material a suitable candidate for device applications.

To probe the ferroelectric phase transition, we have performed differential scanning calorimetry (DSC) studies from room temperature to 870 K (Fig. 3 (b)). We observed a sharp endothermic peak ~ 700 (± 10) K. The presence of the endothermic peak in DSC thermogram indicates that the ferroelectric–paraelectric phase transition occurs around 700 (± 10) K. The occurrence of the endothermic transition is corroborated by Raman studies.

The existence of ferroelectricity in PZTNi30 ceramics is examined by measuring electrical polarization (P) versus electric field (E) hysteresis loops at room temperature for poled and unpoled sample at a frequency of 2 Hz (Fig 3 (c)). The ferroelectric measurements were performed

after poling the sintered pellet electrically at 12 kV/cm for 6 h. Both the unpoled and poled samples exhibit well saturated square hysteretic behavior with saturation polarization (P_s) 9.5, 12.5 (± 0.5) μC/cm^2, remanent polarization (P_r) 5.1, 8.7 (± 0.5) μC/cm^2, and coercive field (H_c) 8.25 and 9.5, (± 0.5) kV/cm respectively, with the maximum applied electric field of 25 kV/cm. The P_s, P_r and H_c values of poled samples are found to be higher than the unpoled samples.

The leakage current characteristics of PZTNi30 samples have been studied by electric field (E) dependence of current density (J) measurements (Fig 3 (d)). The J - E curve shows that PZTNi30 possesses low leakage current and symmetrical behavior under positive and negative electric fields up to ± 6 kV/cm. But a rapid increase in the leakage current with increase of applied electric field can be seen in the J-E curve. The leakage current density of PZTNi30 ceramic was observed to be 1.08 $\times 10^{-9}$ A/cm^2 without very small applied field but 4.5×10^{-7} A/cm^2 with the maximum applied electric field of 6 kV/cm. The leakage current observed in our sample is found to be lower than $BiFeO_3$.[30] As the room temperature leakage current and loss tangent of PZTNi30 are found to be low, good ferroelectric behavior has been observed and strong ME coupling is expected.

Raman Spectroscopic Studies:

Raman scattering is sensitive to local heterogeneities, which are related to the compositional and structural disorder, and the structural phase transitions of ferroelectrics, relaxor ferroelectrics as well as multiferroic materials.[31-33] Temperature dependence of Raman scattering spectra have been investigated to probe the ferroelectric phase transition and to understand the phonon dynamics of PZTNi30 ceramics. In the analysis of Raman spectra, the reduced intensity $I^r(\omega)$ was calculated from the Stokes component of the observed Raman scattering intensity $I(\omega)$ by the following equation to avoid the effect of Bose-Einstein phonon population:[25,26]

$$I^r(\omega) = \frac{I(\omega)}{\omega[n(\omega)+1]} \quad \text{..... (1)}$$

where, $n(\omega) = \frac{1}{\exp\left(\frac{\hbar\omega}{k_B T}\right)-1}$ is the Bose-Einstein population factor, in which k_B and $\hbar$ are the Boltzmann and Dirac constants, respectively. The temperature dependence of the reduced Raman spectra of the PZTNi30 ceramic is shown in Fig. 4(a). In order to understand the phonon dynamics and to clarify the ferroelectric phase transition that was not observed in the dielectric spectroscopy due to experimental limitations, all reduced spectra were fitted in the frequency range 12 ~ 320 cm^{-1} by the combination of a Lorentzian central peak (CP) and damped harmonic oscillator (DHO) model by the following equation:[25,34-35]

$$I^r(\omega) = \frac{2A_{CP}}{\pi}\frac{\Gamma_{CP}}{4\omega^2 + \Gamma_{CP}^2} + \sum_i \frac{A_i\Gamma_i\omega_i^2}{\left(\omega^2-\omega_i^2\right)^2+\omega^2\Gamma_i^2} \quad \text{..... (2)}$$

where, A_{CP} and Γ_{CP} are intensity and full width at half maximum (FWHM) of the CP, respectively. ω_i, Γ_i, and A_i are frequency, damping constant, and intensity of the ith Raman active optical mode, respectively. The example of a fit of Raman spectrum using Eq. (2) is shown in Fig. 4(b). The detailed assignment of Raman modes of the PZT were reported elsewhere.[29,36] At 263 K, the frequencies of various Raman modes of the PZTNi30 have been found at 48, 68, 104, 145, 197, 206, and 280 cm^{-1} as shown in Fig. 4(b). In the cubic phase of $PbTiO_3$ and in cubic phase of $PbTiO_3$, the optic modes transform as the $3T_{1u}+T_{2u}$ irreducible presentations of the space group $Pm\bar{3}m$. The three triply degenerate T_{1u} modes are infrared active, whereas the triply degenerate T_{2u} mode is both infrared and Raman inactive (often called a "silent mode"). In the tetragonal ferroelectric phase with *P4mm* symmetry, all the phonons become Raman-active. Each of the T_{1u} mode splits into modes of symmetry A_1+E, and the T_{2u} mode splits into modes of B_1+E symmetry in tetragonal phase. Here we are mainly concerned about the low frequency Raman modes of the

PZTNi30 ceramic. In ceramics, no direct assignments of mode symmetries are possible from the Raman measurements. Therefore, we follow our assignments of mode symmetries as in PZT35 single crystals.[29] It is seen that the Raman spectra of the PZTNi30 consist of mainly E(1TO) (~ 60 cm^{-1}), E(1LO) (~104 cm^{-1}), A_1(1TO) (~145 cm^{-1}), E(2TO) (~200 cm^{-1}), and E(3TO) + B_1 doublet (~280 cm^{-1}) in the frequency range of 12~320 cm^{-1}, as shown in Fig. 4(b). It is important to note that the E(1TO) and E(1TO) modes each split into two modes denoted as $E(1TO)_1$ (48 cm^{-1}) and $E(1TO)_2$ (68 cm^{-1}), and $E(2TO)_1$ (197 cm^{-1}) $E(2TO)_2$ (206 cm^{-1}) (Fig. 4(b)). The splitting of the transverse E modes can be due to the different local order regions in PZTNi30 ceramic (e.g., slight orthorhombic symmetry).[29] Another possibility of the splitting of E modes might be due to the partial occupancy of few percentage of Ni at A-site in Ni-rich PZT. The partial occupancy of the Ni at both A- and B-site has been discussed in the theory section. In the low-frequency region, the following variations were observed in the spectra upon heating: (i) most of the intense modes shift toward lower frequency; (ii) most of the modes broaden; and (iii) mode intensities diminish and disappear completely for only one phonon branch at around 104 cm^{-1} as the temperature approaches at the ferroelectric to paraelectric phase transition temperature (T_c) (Fig. 4). These observations can be described by anharmonic lattice effects, thermal broadening and thermal disorder. In addition, the change in bond length between cations and oxygen (thermal expansion) will decrease vibrational frequencies with increasing temperature. All Raman modes show changes in their lineshapes; but for clarity we show only the frequency and FWHM of $E(1TO)_1$, $E(1TO)_1$, and E(1LO) modes. The temperature dependence of frequency and FWHM of these modes are plotted in Figs. 4(c) and 4(d), respectively. Note that the frequency of the E(1LO) mode shifts significantly toward lower frequency with increasing temperature and disappears above T_c = 703 ± 10 K, while the frequency of $E(1TO)_1$, and $E(1TO)_2$ modes show slight softening and a clear

anomaly at around T_c. The FWHM of Raman modes exhibits a clear anomaly at about T_c as well (Fig. 4(d)). The complete disappearance and the anomalous change of Raman modes at around T_c were reported in different types of materials such as ferroelectric and multiferroic materials.[23,25,26] It also significant that the FWHM of these modes increases gradually with temperature as the temperature approaches T_c , albeit the FWHM of the *E*(1LO) mode is decreased in the vicinity of the T_c, implying some order-disorder character of the ferroelectric phase transition of the PZTNi30 ceramic. In inelastic light scattering the ferroelectric soft mode is a general property of a crystals/ceramics undergoing a displacive phase transition, while the CP is a common feature of the order-disorder phase transition. Fontana *et al*. reported the coexistence of the displacive and the order-disorder phase transition in $KNbO_3$ by the observation of the soft mode and the CP using Raman scattering.[37] In the present study, the soft mode of the PZTNi30 ceramic was not observed. However, the prominent CP was clearly observed in the vicinity of the T_c of the PZTNi30 ceramic as shown in Fig. 4(a). Therefore, the existence of the broad CP can be the clear evidence of the order-disorder nature of the ferroelectric phase transition of the PZTNi30 ceramic. According to the Raman selection rules, first-order Raman modes are prohibited in the paraelectric cubic phase with $Pm\bar{3}m$ symmetry. However, these first-order modes still exist in the paraelectric cubic phase, as shown in Fig. 4(c). Therefore, the existence of the first order mode in the paraelectric phase demonstrates the local mon-cubic symmetry breaking. The local symmetry breaking could be due to octahedral tilting and/or polar distortions/fluctuations.[23,25,26] The disappearance of the Raman modes above a certain temperature shows that either the material has decomposed and become amorphous or it transformed via a structural phase transition to its cubic phase. We tested the possibility of the former case by recording the Raman spectra by cooling it to room temperature

and observed all the peaks distinctly reappear, which ruled out the probability of decomposition of the sample and indicated that the sample indeed transformed to a cubic phase above T_c.[23]

Magnetic Properties:

To prove the existence of magnetic orderings above room temperature, dc-magnetization measurements as a function of temperature (M-T) and magnetic field (M-H) have been carried out and depicted in Figure 5. All the M-T and M-H measurements were performed in the in-plane (magnetic field parallel to the surface of the sample) configuration. Field-cooled (FC) and zero-field-cooled (ZFC) magnetic measurements as a function of temperature were carried out under an external dc field of 100 Oe in the temperature range of 300 - 800 K (Fig. 5(a)). We found faint bifurcation in ZFC-FC curve which indicates that PZTNi30 has less magnetic frustration in the system, since ZFC - FC bifurcation signifies the presence of a magnetic instability.[23] The magnetization decreases slowly up to 550 K and then decreases suddenly with the increase of temperature and is almost constant above ~ 625 K but does not vanish completely. The estimated magnetic transition temperature for PZTNi30 is observed around 602 (± 10) K with a relaxor paramagnetic back ground.

The magnetic properties of PZTNi30 were further analyzed by measuring the magnetic moment as a function of magnetic field (M-H loops) at different temperature shown in Fig. 5 (b, c, d). The M-H loop measured at room temperature shows weak ferromagnetic behavior having remanent magnetization (M_r) of 1.9 (± 0.1) $\times 10^{-4}$ emu/g and coercive field (H_c) of 112 (± 2) Oe. With increase of temperature, M_s and M_r are found to decrease, as can be seen from Fig. 5(c), without the complete saturation of magnetization. Fig. 5(c) and (d) show the M-H loops of PZTNi30 ceramics before (500 K) and after the phase transition (635 K), where the M-H loop

taken at 635 K shows paramagnetic behavior. From both figures it is clear that PZTNi30 indeed undergoes a ferromagnetic to paramagnetic transition. The observed magnetic behavior in PZTNi30 is assumed due to the substitution of Ni^{2+} into the host lattice. Similar phenomena were also observed in other transition metal (Fe and Mn) doped $PbTiO_3$ perovskites.[38-39]

Magnetoelectric coupling

Existence of coupling between the electrical and magnetic order parameters in PZTNi30 ceramics was investigated by measuring magnetoelectric voltage coefficients (α_{ME}) via a dynamic method at low frequencies.[40] The sample was initially poled electrically at ~ 6 kV/cm at room temperature for 4 h. Here we measured the change in electric field produced by an alternating magnetic field applied to the sample surface. In the ME measurement set-up the sample was subjected to a bias field H by using an electromagnet and an ac magnetic field δH (1 Oe) produced by a pair of Helmholtz coils and lock-in detection for measuring the ME voltage δV generated across the sample thickness. The measurements were carried out for in-plane mode for H and δH parallel to each other and to the sample plane (along direction *1*) and perpendicular to δE along direction *3* (termed transverse orientation α_{31}). The transverse ME voltage coefficient ($\alpha_{E,31}$) was measured as a function of static magnetic field (H = 0 - +3000 Oe) with ac field (δH) varying from 1- 10 Oe with frequencies ranging from 30-100 Hz and at room temperature (Fig. 6). Fig.6 (a) and (b) shows the magnetic field dependence of $\alpha_{E,31}$ at ac magnetic field (H_{ac}) of 1 and 3 Oe at constant frequency of 30 Hz and 1 kHz. The magnitude of $\alpha_{E,31}$ is almost constant with increasing H. With increase of H_{ac} the magnitude of $\alpha_{E,31}$ decreases. PZTNi30 exhibits a $\alpha_{E,31}$ ~ 1.25 mV/cm.Oe at H_{ac} =1 Oe (Fig.6 (a)) and increases to ~ 11.6 mV/cm.Oe (Fig.6 (b)) with increase of frequency from 30 Hz to 1 kHz. The ME coupling coefficient of PZTNi30 is found to be higher than

$Bi_{0.68}Pb_{0.32}Fe_{0.655}Mn_{0.025}Ti_{0.32}O_3$ ($\alpha_{E,31}$ = 0.5 mV/cm.Oe (at 10Oe and 100 kHz)), $BiFeO_3$ ($\alpha_{E,31}$ = 0.29 mV/cm.Oe), $Bi_{0.7}Sr_{0.3}FeO_3$ ($\alpha_{E,31}$ = 0.37 mV/cm.Oe), $Pb(Zr_{0.20}Ti_{0.80})_{0.70}Pd_{0.30}O_{3-\delta}$ ($\alpha_{E,31}$ = 0.36 mV/cm.Oe (at 1Oe and 100 Hz)), $Bi_{1-x}Nd_xFe_yMn_{1-y}O_3$, $Bi_{1-x}Nd_xFeO_3$ and $(BiFeO_3)_{1-x}-(BaTiO_3)_x$ solid solutions which show maximum α_{ME} is of the order of 1.0-2.7 mV/cm.Oe and lower than $Sr_3Co_2Fe_{24}O_{41}$ ($\alpha_{E,31}$ = 15 mV/cm.Oe (at 2Oe and1 kHz)).[12, 41-45] The observed strong ME coupling in PZTNi30 may arise because this system exhibit large polarization and weak ferromagnetism and perhaps also due to the close proximity between the ferroelectric and magnetic ordering temperatures ($T_{c\ (FE)}$ ~ 700 K and $T_{c\ (Magnetic)}$ ~ 602 K). The existence of strong ME coupling has been theoretically proposed and experimentally observed in the materials which exhibit less independence between ferroelectric and magnetic ordering temperature. Observation of strong ME coupling in PZTNi30 might be due to the local sub-lattice interactions between spin moments and the disordered electric dipole moment.[1,2,5] The presence of strong room-temperature ME coupling makes it promising material for memory, spintronics and other multifunctional device applications.

Theory

A bond magnetic polaron model was proposed to explain the magnetization in transition metal-doped ferroelectrics[46]. It was suggested that in Ni-doped PZT ceramics, some bound electrons arise from the oxygen vacancies (V_O^{2-}) which are being created to maintain the charge neutrality, and with oxygen loss during the synthesis. The Ni^{2+} ions and the localized electrons might form bound magnetic polarons. The bound electron occupies a Bohr orbit, and as a bound polaron, it mediates ferromagnetic ordering of Ni within this orbital volume. The electron embedded in the oxygen vacancy occupies an orbital that overlaps the d-shells of both Ni^{2+} neighbors. A ferromagnetic exchange interaction between the magnetic Ni^{2+} ions and a spin-polarized electron trapped at

oxygen vacancy (Ni^{2+} –V_O^{2-} –Ni^{2+} groups) can occur.[34] However, this model has not been convincingly demonstrated quantum mechanically.

We carried out first-principle density functional theory (DFT) calculations to understand the origin of magnetism in Ni-doped PZT. Given the chemical similarity between PZT and $PbTiO_3$, we consider Ni-doped $PbTiO_3$ as a model system for DFT investigations where a 2×2×2 supercell is used. We investigate both point defects and dipolar defects: 1) substitute two Ti or Pb cations with Ni isovalently leading to charge neutral defects $(Ni_{Ti})^{\times}$ and/or $(Ni_{Pb})^{\times}$; 2) replace Ti^{4+} with Ni^{2+} coupled with a nearby charge-compensating oxygen vacancy, leading to a dipolar defect $[(Ni_{Ti}'' - V_O^{\cdot\cdot})^{\times}]$. The lattice constants are fixed to experimental values and the atomic positions are fully relaxed. We calculate the energy difference between the ferromagnetic and antiferromagnetic states for all 28 possible configurations and find surprisingly that only when the two Ni dopants replace two Pb atoms, the Ni-doped PTO adopts a magnetic ground state. The lowest energy configuration has two Ni atoms being the nearest neighbors and Ni-Ni aligned mostly along the *c* direction (Fig. 7a). Figure 7b presents the atomic orbital-resolved density of states which reveals a semiconducting behavior with a band gap of 1.86 eV. Interestingly, we find that only one Ni is spin polarized (labeled as Ni1 in Figure 7a) with a local magnetic moment of $1.68\mu_B$ whereas the other Ni atom is not spin-polarized with a local magnetic moment close to zero. This can be understood by the crystal field theory. As shown in Figure 7a, Ni1 is coordinated by five oxygen atoms (with Ni-O bond length < 3.0 Å), and thus experiences a square pyramidal crystal field. The Ni1 magnetic moment is $1.68\mu_B$, suggesting a high-spin state and an oxidation state of +2. In comparison, Ni2 is in a square planar crystal field as it has only four nearby oxygen atoms and eventually adopts a low-spin state with zero magnetic moment (Figure 7c). It is noted that this magnetic state is 0.21 eV lower than the antiferromagnetic state where both Ni atoms are

spin polarized, which may explain the very large magnetic Curie temperature observed experimentally. We propose that the presence of a mixed high-spin and low-spin states in Ni-doped $PbTiO_3$ is responsible for the magnetization.

We further explore the effects of strain on the ferromagnetic-antiferromagnetic energy difference ($\Delta E = E_{FM} - E_{AFM}$) and the local magnetic moments on Ni atoms. As shown in the two-dimensional map of ΔE as a function of tetragonal lattice parameters (a, c), the magnetic state has lower energy for all strain conditions explored. We also quantify the effects of microscopic strain on the magnitude of magnetization by mapping out $(\mu-\mu_0)/\mu_0$ vs (a, c), where μ is the local magnetic moment of Ni and $\mu_0 = 1.68\mu_B$ is the value calculated with experimental lattice constants. It is found that a few percent change in magnetization can be realized by modulating strain. Our first-principles investigations suggest the $(Ni_{Pb})^{\times}$ defect is likely to be responsible for the experimental ME coupling in Ni-doped PZT. The requirement of $(Ni_{Pb})^{\times}$ for magnetization also explains the relatively low magnetization observed experimentally as majority of Ni dopants tend to replace *B*-site cations.

Conclusions:

PZTNi30 single phase ME material having tetragonal crystal structure with *P4mm* symmetry was successfully synthesized for possible room temperature nonvolatile multi-state memory elements and for spintronics devices operated and controlled under external electric and magnetic fields. PZTNi30 exhibits ferromagnetism and ferroelectric ordering temperature well above room temperature with less independence, as shown by the relative closeness of the two ordering temperatures. PZTNi30 possesses low leakage current, large polarization and weak ferromagnetism with high ME coupling coefficient of ~ 1.25 mV/cm.Oe (at H_{ac}=1 Oe, f = 30 Hz)

in a single-phase system, revealing a strong coupling between electrical and magnetic order parameters. The strong ME coupling above room-temperature makes it a possible future alternative of other single phase multiferroics with a strong possibility for device applications.

Acknowledgments

This work was supported by DoD-AFOSR (Grant #FA9550-16-1-0295). J.F.S acknowledges EPSRC grant EP/P024637/1.

Figure Captions

Fig. 1. (Color online) The Rietveld refined XRD patterns of PZTNi30 ceramics using Fullprof Suite Software.

Fig. 2. (Color online) (a) a typical FESEM micrograph image of PZTNi30 ceramic with elemental mapping of the corresponding area and distribution maps of elements Pb, Zr, Ti, Ni, and O (b) elemental mapping on one grain and distribution maps of elements Pb, Zr, Ti, Ni, and O.

Fig. 3. (Color online) (a) Temperature dependence of relative dielectric permittivity of PZTNi30 ceramics at different frequencies, the inset shows respective temperature dependent of tanδ, (b) DSC thermogram of PZTNi30 ceramics, (c) Ferroelectric (P-E) hysteresis loops of poled and unpoled PZTNi30 at room temperature, (d) Leakage current density (*J*) as function of electric field for PZTNi30 ceramics at room temperature.

Fig. 4. (Color online) (a) The temperature dependence of reduced Raman spectra of PZTNi30 at some selected temperatures. The example of a fit of Raman spectrum at 263 K using the equation (2) is shown in (b), (c) The temperature dependence of the frequency shift of first order modes at around 48 cm^{-1}, 68 cm^{-1}, and 104 cm^{-1} of the PZTNi30 ceramic. (d) The FWHM of the modes at about 48 cm^{-1}, 68 cm^{-1}, and 104 cm^{-1} of the PZTNi30 ceramic as a function of temperature.

Fig. 5. (Color online) (a) ZFC and FC plot of PZTNi30 ceramics at 100 Oe, Magnetic (M-H) hysteresis loops of PZTNi30 at (b) 300 K (c) 500 K (d) 635 K respectively.

Fig. 6. (Color online) Magnetoelectric coupling coefficients (a) as a function of an externally applied magnetic field (a) at H_{ac} of 1 and 3 Oe at a frequency of 30 Hz (b) (a) at H_{ac} of 1, 5 and 10 Oe at a frequency of 1k Hz of PZTNi30 at room temperature.

Fig. 7. (a) 2×2×2 $PbTiO_3$ supercell with two $(Ni_{Pb})^{\times}$ defects. (b) Atomic orbital-resolved density of states. (c) Square planar crystal field splitting diagram. Two-dimensional plot of (d) ferromagnetic-antiferromagnetic energy difference (ΔE) and (e) change in local magnetic moment of Ni atoms $(\mu-\mu_0)/\mu_0$ as a function of tetragonal lattice parameters.

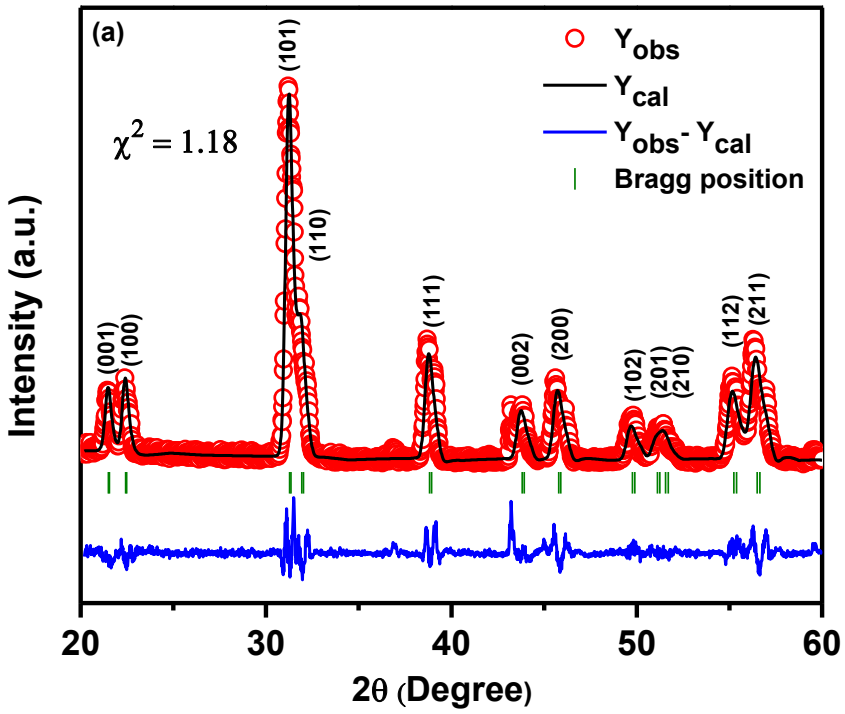

Figure 1. Kumari et al.

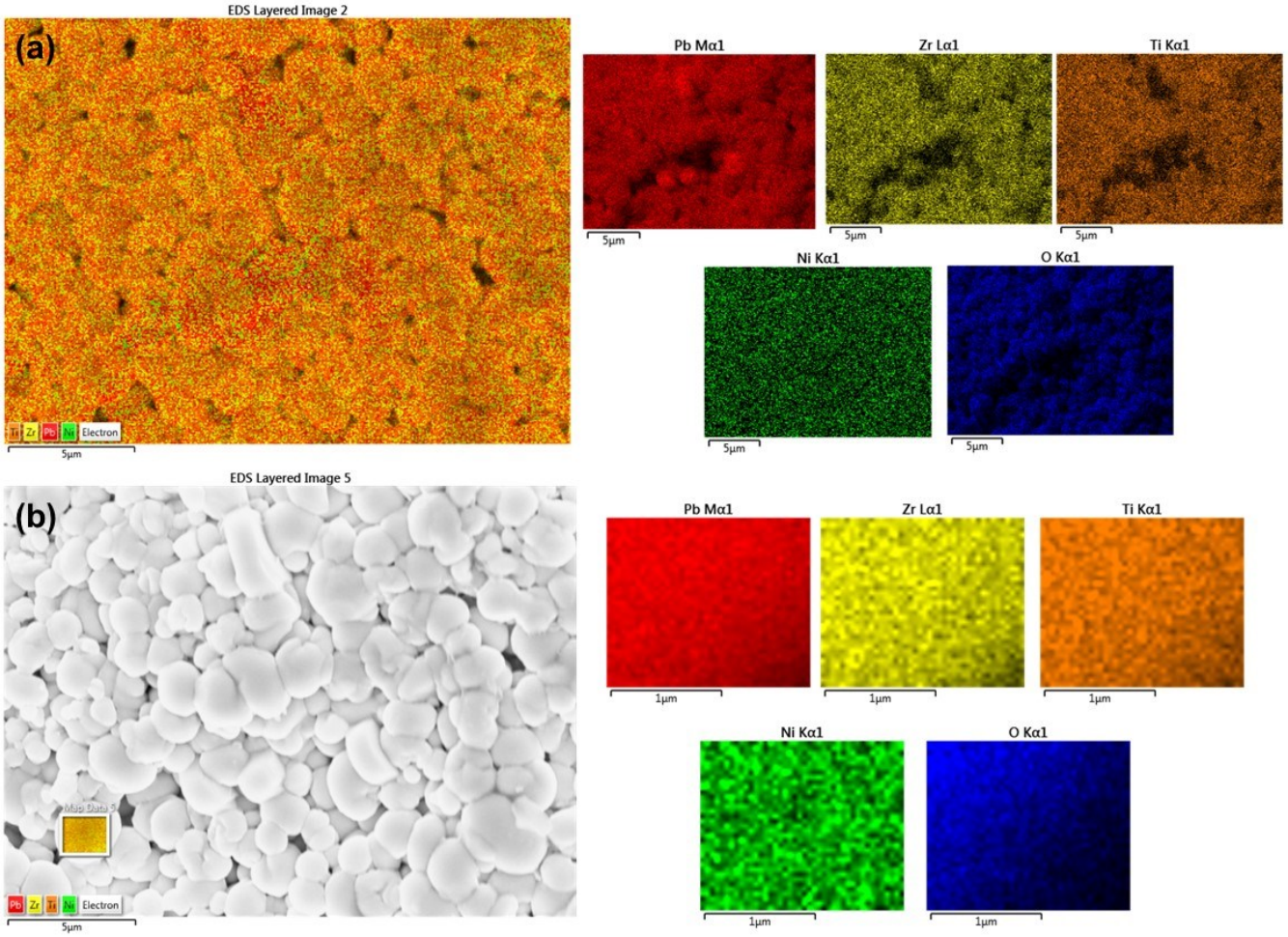

Figure 2. Kumari et al.

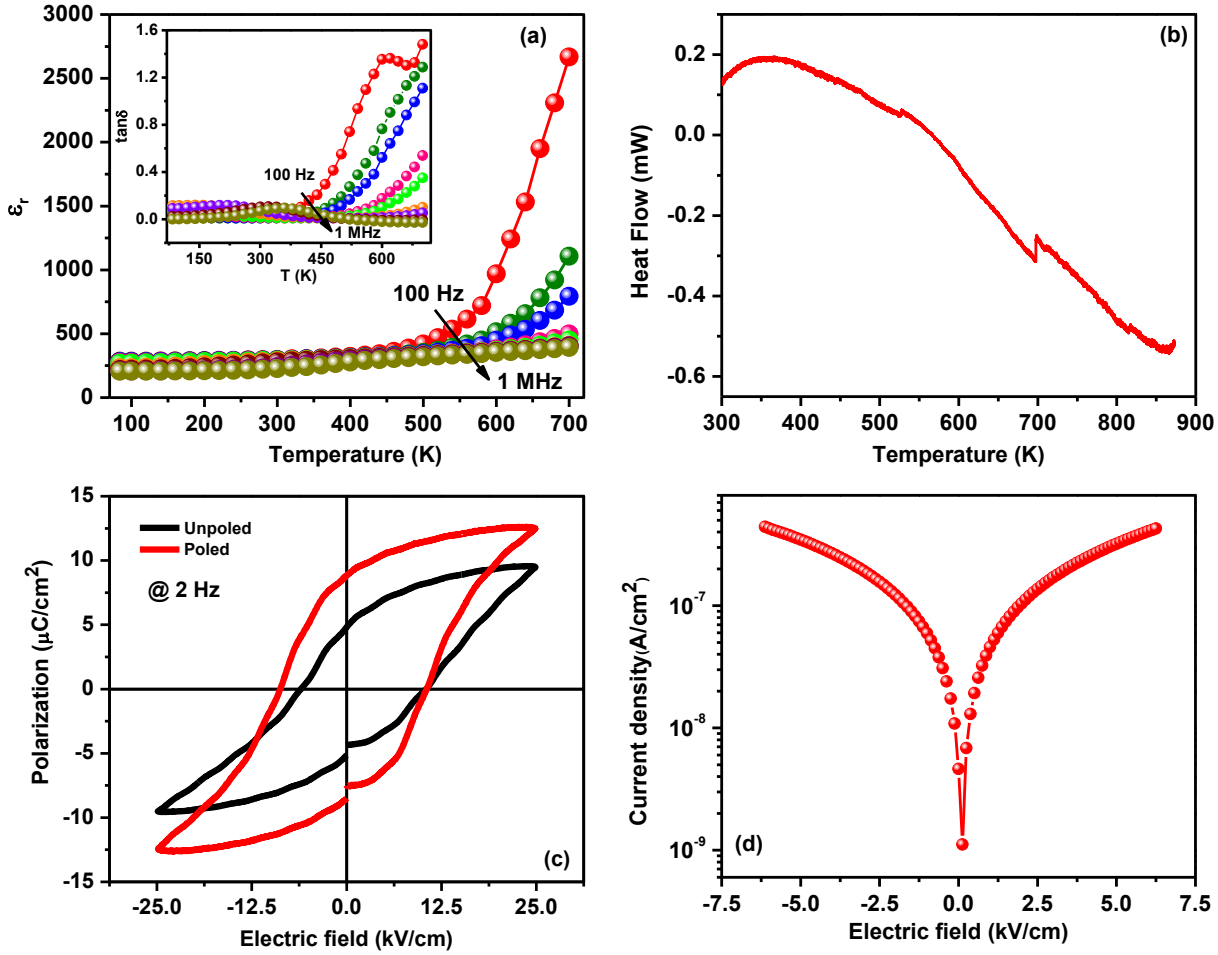

Figure 3. Kumari et al.

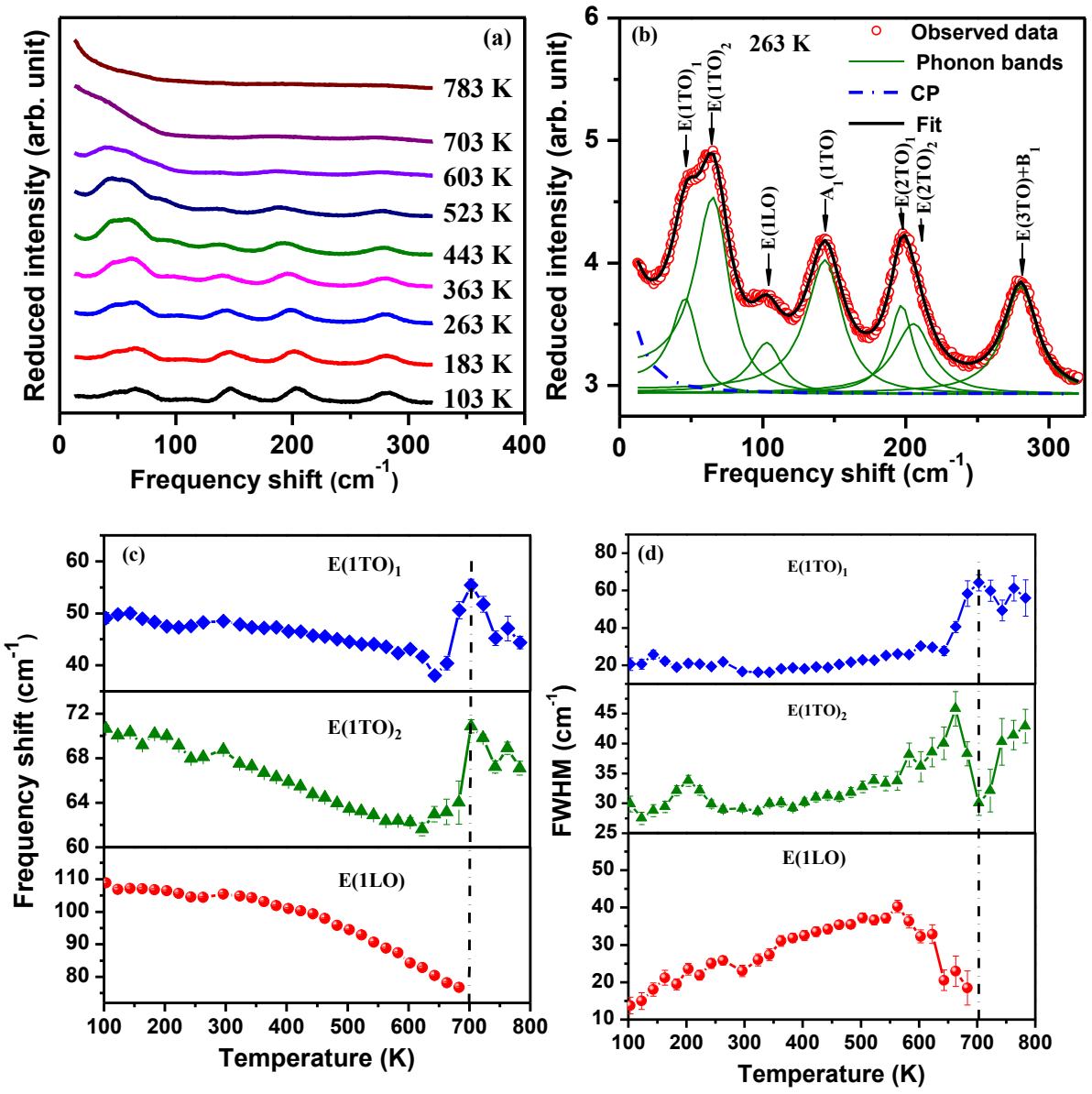

Figure 4. Kumari et al.

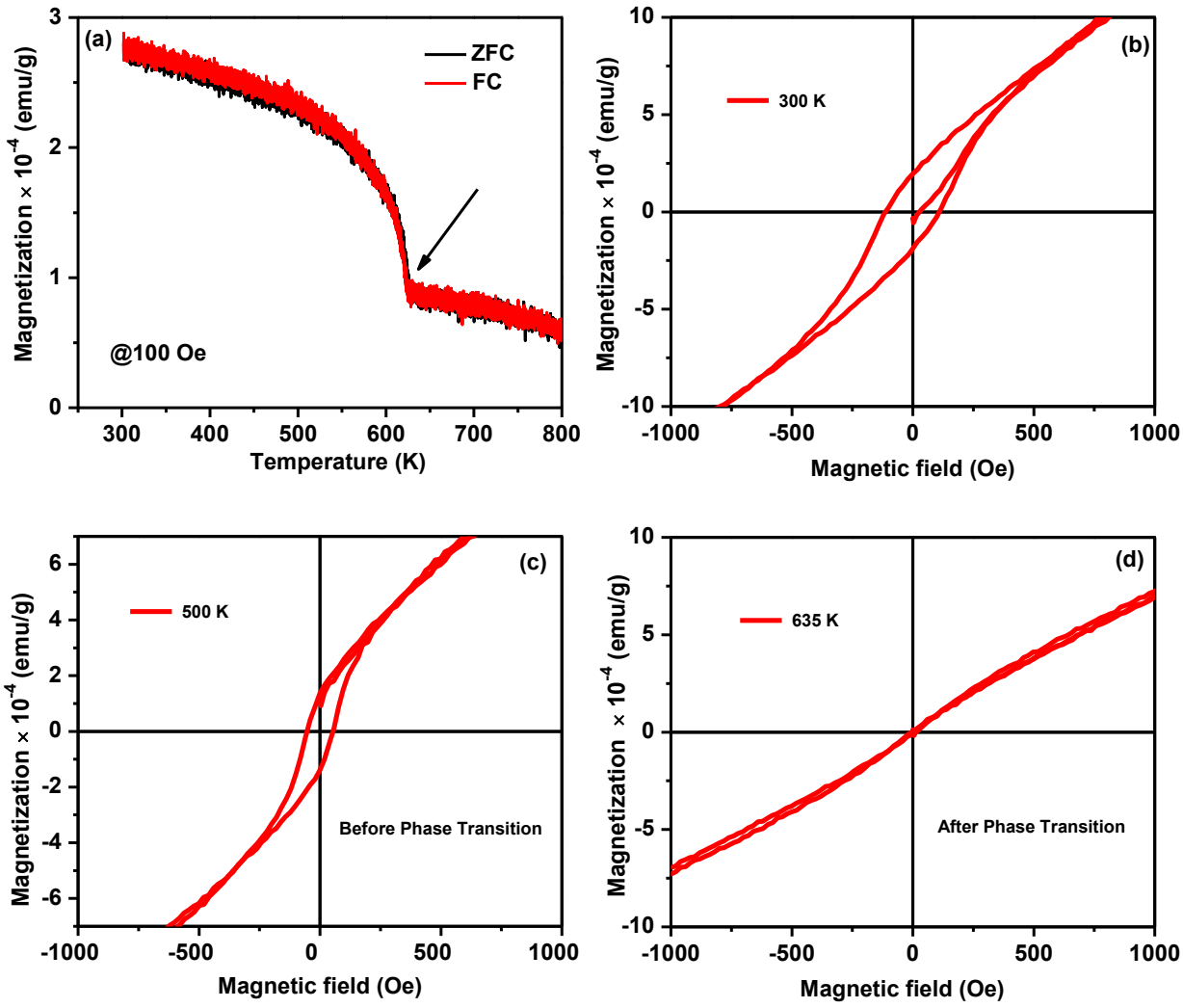

Figure 5. Kumari et al.

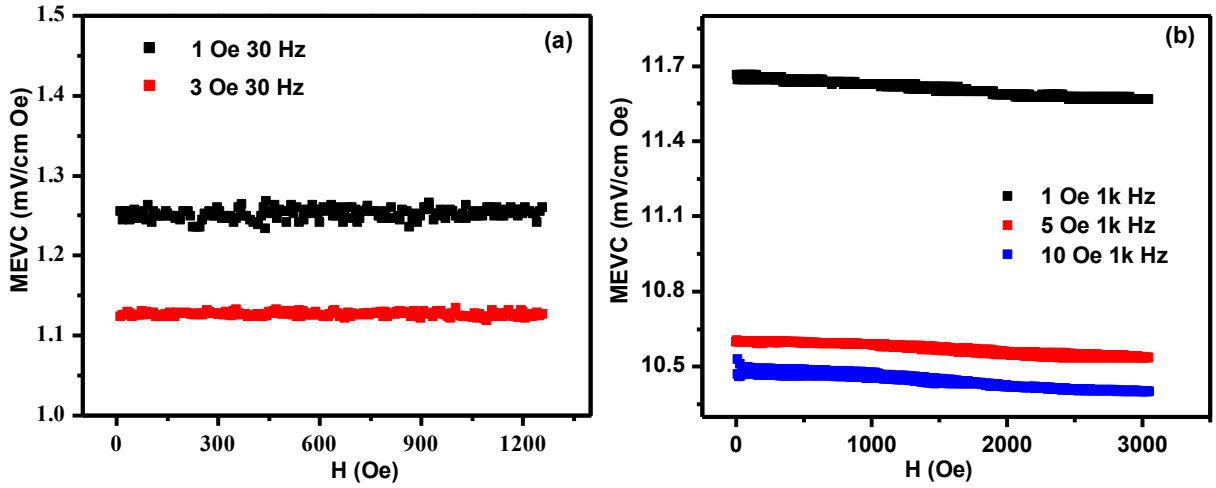

Figure 6. Kumari et al.

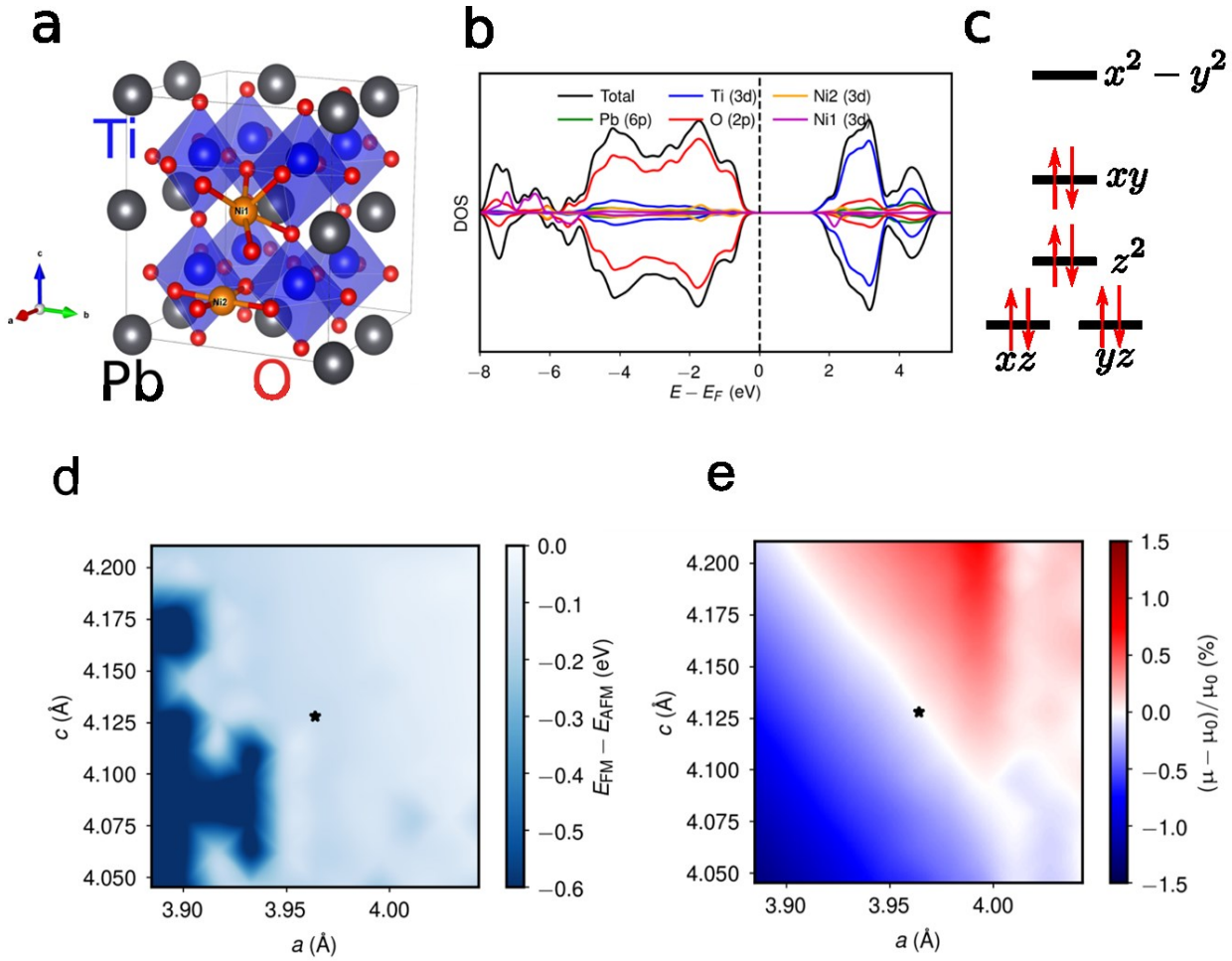

Figure 7. Kumari et al.

Table 1

Molecular formula	$Pb(Zr_{0.20}Ti_{0.80})_{0.70}Ni_{0.30}O_{3-\delta}$
Difractometer	Rigaku Ultima III (to check)
CuKα radiation	λ=1.5405 Å (to check)
Scan mode	θ-2θ
2θ range	20-80°
Scan width-scan speed	0.02, 0.2° min^{-1}
Crystal Symmetry	Tetragonal
Space group	*P4mm*
Unit cell parameters	a =b= 3.9602, c=4.1289Å
	α= β= γ= 90°
Volume	64.4505 $Å^3$
Density	6.011 g/cm^3
Profile function	Pseudo-Voigt
FWHM parameters (U, V and W)	0.04136 -0.01574 0.01453
Preferred orientation parameters	0.000000 0.000000 0.000000
Pattern residual (R_p)	19.5
Weighted pattern residual (R_{wp})	13.3
Expected residual (R_{exp})	11.0
Bragg factor (R_B)	3.72
Structural factor (R_F)	2.54
Chi^2	1.18

1. Eerenstein, W.; Mathur, N.; Scott, J. F., Multiferroic and magnetoelectric materials. *nature* **2006,** *442* (7104), 759-765.
2. Fiebig, M., Revival of the magnetoelectric effect. *Journal of Physics D: Applied Physics* **2005,** *38* (8), R123.
3. Scott, J., Data storage: Multiferroic memories. *Nature materials* **2007,** *6* (4), 256.
4. Bibes, M.; Barthélémy, A., Multiferroics: Towards a magnetoelectric memory. *Nature materials* **2008,** *7* (6), 425.
5. Martin, L.; Chu, Y.-H.; Ramesh, R., Advances in the growth and characterization of magnetic, ferroelectric, and multiferroic oxide thin films. *Materials Science and Engineering: R: Reports* **2010,** *68* (4-6), 89-133.
6. Waldrop, M. M., The chips are down for Moore's law. *Nature News* **2016,** *530* (7589), 144.
7. Hill, N. A., Why are there so few magnetic ferroelectrics? ACS Publications: 2000.
8. Spaldin, N. A.; Cheong, S.-W.; Ramesh, R., Multiferroics: past, present, and future. *Physics Today* **2010,** *63* (10), 38-43.
9. Catalan, G.; Scott, J. F., Physics and applications of bismuth ferrite. *Advanced Materials* **2009,** *21* (24), 2463-2485.
10. Palai, R.; Katiyar, R.; Schmid, H.; Tissot, P.; Clark, S.; Robertson, J.; Redfern, S.; Catalan, G.; Scott, J., β phase and γ− β metal-insulator transition in multiferroic Bi Fe O 3. *Physical Review B* **2008,** *77* (1), 014110.
11. Evans, D. M.; Alexe, M.; Schilling, A.; Kumar, A.; Sanchez, D.; Ortega, N.; Katiyar, R. S.; Scott, J. F.; Gregg, J. M., The nature of magnetoelectric coupling in Pb (Zr, Ti) O3–Pb (Fe, Ta) O3. *Advanced Materials* **2015,** *27* (39), 6068-6073.

12. Kumari, S.; Pradhan, D. K.; Ortega, N.; Pradhan, K.; DeVreugd, C.; Srinivasan, G.; Kumar, A.; Paudel, T. R.; Tsymbal, E. Y.; Bumstead, A. M., Palladium-based ferroelectrics and multiferroics: Theory and experiment. *Physical Review B* **2017,** *95* (21), 214109.
13. Li, Y.; Wang, Z.; Yao, J.; Yang, T.; Wang, Z.; Hu, J.-M.; Chen, C.; Sun, R.; Tian, Z.; Li, J., Magnetoelectric quasi-(0-3) nanocomposite heterostructures. *Nature communications* **2015,** *6*, 6680.
14. Ma, J.; Hu, J.; Li, Z.; Nan, C. W., Recent progress in multiferroic magnetoelectric composites: from bulk to thin films. *Advanced Materials* **2011,** *23* (9), 1062-1087.
15. Wang, Y.; Hu, J.; Lin, Y.; Nan, C.-W., Multiferroic magnetoelectric composite nanostructures. *NPG Asia Materials* **2010,** *2* (2), 61.
16. Pradhan, D. K.; Puli, V. S.; Kumari, S.; Sahoo, S.; Das, P. T.; Pradhan, K.; Pradhan, D. K.; Scott, J. F.; Katiyar, R. S., Studies of Phase Transitions and Magnetoelectric Coupling in PFN-CZFO Multiferroic Composites. *The Journal of Physical Chemistry C* **2016,** *120* (3), 1936-1944.
17. Nan, C.-W.; Bichurin, M.; Dong, S.; Viehland, D.; Srinivasan, G., Multiferroic magnetoelectric composites: Historical perspective, status, and future directions. *Journal of Applied Physics* **2008,** *103* (3), 1.
18. Fusil, S.; Garcia, V.; Barthélémy, A.; Bibes, M., Magnetoelectric devices for spintronics. *Annual Review of Materials Research* **2014,** *44*, 91-116.
19. Kumari, S.; Pradhan, D. K.; Katiyar, R. S.; Kumar, A., Ferroelectric, ferromagnetic, and multiferroic heterostructures for possible applications as tunnel junctions. In *Magnetic, Ferroelectric, and Multiferroic Metal Oxides*, Elsevier: 2018; pp 571-591.
20. Heine, V.; Joynt, R., Coarse-grained magnetic disorder above Tc in iron. *EPL (Europhysics Letters)* **1988,** *5* (1), 81.
21. Kumari, S.; Ortega, N.; Kumar, A.; Scott, J.; Katiyar, R., Ferroelectric and photovoltaic properties of transition metal doped Pb (Zr0. 14Ti0. 56Ni0. 30) O3-δ thin films. *AIP Advances* **2014,** *4* (3), 037101.
22. Kumari, S.; Ortega, N.; Pradhan, D. K.; Kumar, A.; Scott, J. F.; Katiyar, R. S., Effect of thickness on dielectric, ferroelectric, and optical properties of Ni substituted Pb (Zr0. 2Ti0. 8) O3 thin films. *Journal of Applied Physics* **2015,** *118* (18), 184103.
23. Giannozzi, P.; Baroni, S.; Bonini, N.; Calandra, M.; Car, R.; Cavazzoni, C.; Ceresoli, D.; Chiarotti, G. L.; Cococcioni, M.; Dabo, I., QUANTUM ESPRESSO: a modular and open-source software project for quantum simulations of materials. *Journal of physics: Condensed matter* **2009,** *21* (39), 395502.
24. Garrity, K. F.; Bennett, J. W.; Rabe, K. M.; Vanderbilt, D., Pseudopotentials for high-throughput DFT calculations. *Computational Materials Science* **2014,** *81*, 446-452.
25. Anisimov, V. I.; Zaanen, J.; Andersen, O. K., Band theory and Mott insulators: Hubbard U instead of Stoner I. *Physical Review B* **1991,** *44* (3), 943.
26. Cococcioni, M.; De Gironcoli, S., Linear response approach to the calculation of the effective interaction parameters in the LDA+ U method. *Physical Review B* **2005,** *71* (3), 035105.
27. Rodríguez-Carvajal, J., Recent advances in magnetic structure determination by neutron powder diffraction. *Physica B: Condensed Matter* **1993,** *192* (1-2), 55-69.
28. Sani, A.; Hanfland, M.; Levy, D., The equation of state of PbTiO3 up to 37 GPa: a synchrotron x-ray powder diffraction study. *Journal of Physics: Condensed Matter* **2002,** *14* (44), 10601.
29. Pradhan, D. K.; Misra, P.; Puli, V. S.; Sahoo, S.; Pradhan, D. K.; Katiyar, R. S., Studies on structural, dielectric, and transport properties of Ni0. 65Zn0. 35Fe2O4. *Journal of Applied Physics* **2014,** *115* (24), 243904.
30. Abe, K.; Sakai, N.; Takahashi, J.; Itoh, H.; Adachi, N.; Ota, T., Leakage current properties of cation-substituted BiFeO3 ceramics. *Japanese Journal of Applied Physics* **2010,** *49* (9S), 09MB01.
31. Rahaman, M.; Imai, T.; Sakamoto, T.; Tsukada, S.; Kojima, S., Fano resonance of Li-doped KTa 1− x Nb x O 3 single crystals studied by Raman scattering. *Scientific reports* **2016,** *6*, 23898.

32. Rahaman, M. M.; Imai, T.; Sakamoto, T.; Al Helal, M.; Tsukada, S.; Kojima, S., Ferroelectric phase transition of Li-doped KTa1-xNbxO3 single crystals with weak random fields: Inelastic light scattering study. *Journal of Alloys and Compounds* **2018,** *735*, 1063-1070.
33. Pradhan, D. K.; Sahoo, S.; Barik, S. K.; Puli, V. S.; Misra, P.; Katiyar, R. S., Studies on magnetoelectric coupling in PFN-NZFO composite at room temperature. *Journal of Applied Physics* **2014,** *115* (19), 194105.
34. Toulouse, J.; Jiang, F.; Svitelskiy, O.; Chen, W.; Ye, Z.-G., Temperature evolution of the relaxor dynamics in Pb (Zn 1⁄ 3 Nb 2⁄ 3) O 3: A critical Raman analysis. *Physical Review B* **2005,** *72* (18), 184106.
35. Frantti, J.; Fujioka, Y.; Puretzky, A.; Xie, Y.; Ye, Z.-G.; Glazer, A., A statistical model approximation for perovskite solid-solutions: A Raman study of lead-zirconate-titanate single crystal. *Journal of Applied Physics* **2013,** *113* (17), 174104.
36. Souza Filho, A.; Lima, K.; Ayala, A.; Guedes, I.; Freire, P.; Melo, F.; Mendes Filho, J.; Araujo, E.; Eiras, J., Raman scattering study of the PbZr 1− x Ti x O 3 system: Rhombohedral-monoclinic-tetragonal phase transitions. *Physical Review B* **2002,** *66* (13), 132107.
37. Fontana, M.; Ridah, A.; Kugel, G.; Carabatos-Nedelec, C., The intrinsic central peak at the structural phase transitions in KNbO3. *Journal of Physics C: Solid State Physics* **1988,** *21* (34), 5853.
38. Nakayama, H.; Katayama-Yoshida, H., Theoretical Prediction of Magnetic Properties of Ba (Ti1-xMx) O3 (M= Sc, V, Cr, Mn, Fe, Co, Ni, Cu). *Japanese journal of applied physics* **2001,** *40* (12B), L1355.
39. Keith, G. M.; Rampling, M. J.; Sarma, K.; Alford, N. M.; Sinclair, D., Synthesis and characterisation of doped 6H-BaTiO3 ceramics. *Journal of the European Ceramic Society* **2004,** *24* (6), 1721-1724.
40. Srinivasan, G.; Rasmussen, E.; Gallegos, J.; Srinivasan, R.; Bokhan, Y. I.; Laletin, V., Magnetoelectric bilayer and multilayer structures of magnetostrictive and piezoelectric oxides. *Physical Review B* **2001,** *64* (21), 214408.
41. Naik, V.; Mahendiran, R., Magnetic and magnetoelectric studies in pure and cation doped BiFeO3. *Solid State Communications* **2009,** *149* (19-20), 754-758.
42. Kumari, S.; Ortega, N.; Kumar, A.; Pavunny, S.; Hubbard, J.; Rinaldi, C.; Srinivasan, G.; Scott, J.; Katiyar, R. S., Dielectric anomalies due to grain boundary conduction in chemically substituted BiFeO3. *Journal of Applied Physics* **2015,** *117* (11), 114102.
43. Jartych, E.; Pikula, T.; Kowal, K.; Dzik, J.; Guzdek, P.; Czekaj, D., Magnetoelectric effect in ceramics based on bismuth ferrite. *Nanoscale research letters* **2016,** *11* (1), 234.
44. Fernández-Posada, C. M.; Castro, A.; Kiat, J.-M.; Porcher, F.; Peña, O.; Algueró, M.; Amorín, H., A novel perovskite oxide chemically designed to show multiferroic phase boundary with room-temperature magnetoelectricity. *Nature communications* **2016,** *7*, 12772.
45. Zhai, K.; Shang, D. S.; Chai, Y. S.; Li, G.; Cai, J. W.; Shen, B. G.; Sun, Y., Room‐Temperature Nonvolatile Memory Based on a Single‐Phase Multiferroic Hexaferrite. *Advanced Functional Materials* **2018,** *28* (9), 1705771.
46. Coey, J.; Venkatesan, M.; Fitzgerald, C., Donor impurity band exchange in dilute ferromagnetic oxides. *Nature materials* **2005,** *4* (2), 173.